A Spatially Resolved X-ray Image of a Star Like the Sun

J. H. M. M. Schmitt and M. Kürster

Observations made with the x-ray satellite ROSAT (Roentgen Satellite) have produced the first spatially resolved x-ray image of a corona around a star like our sun. The star is the secondary in the eclipsing binary system α Coronae Borealis (CrB), which consists of one star of spectral type A0V and one of type G5V. The x-ray light curve of α CrB shows a total x-ray eclipse during secondary optical minimum, with the G star behind the A star. The totality of the eclipse demonstrates that the A-type component in α CrB is x-ray dark and that the x-ray flux arises exclusively from the later-type companion. The x-ray eclipse ingress and egress are highly asymmetric compared with the optical eclipse, indicating a highly asymmetric x-ray intensity distribution on the surface of the G star. From a detailed modeling of the ingress and egress of the x-ray light curve, an eclipse map of the G star was constructed by a method based on an optimization by simulated annealing.

Soft x-ray observations with the Einstein and ROSAT satellites in the wavelength range 6 to 100 Å have shown the ubiquitous presence of hot, tenuous coronae around almost all types of stars in the Hertzsprung-Russell diagram (*1, 2*). The only classes of stars that do not appear to be bona fide x-ray emitters are main sequence stars near the spectral range B5 to A5 (*3, 4*) and giant stars close to or beyond a spectral type of K4 (*5–7*). For late-type stars (spectral type A7 and later), the solar corona is usually taken as a model with which we can understand the structure and energetics of stellar coronae (*8*). Spatially resolved x-ray observations show the solar corona to be highly structured and inhomogeneous, with essentially all of the x-ray emission arising in closed magnetic field topologies from archlike structures, which appear to be resolved into smaller scale fibrils (*9, 10*) in higher angular resolution observations.

If the solar analogy indeed applies to the coronae of late-type stars in general, stellar coronae are expected to be structured similar to the solar corona. Stellar coronae cannot be spatially resolved and imaged with presently available x-ray telescopes, so fundamental physical parameters of stellar coronae, such as their filling factors, volumes, pressures, and densities, cannot be directly measured. However, at least some of these physical parameters must be different for stellar coronae, whose total soft x-ray luminosity is known to exceed the solar x-ray output by some orders of magnitude. Without measurements of coronal structure, it is impossible to determine whether this is a result of enhanced volumes (larger loops), filling factors (enhanced area covered by active regions), or densities (larger coronal pressures).

Because of the low spectral resolution of current x-ray detectors [$\lambda/\Delta\lambda \sim 3$ for the ROSAT position-sensitive proportional counter (PSPC)], Doppler imaging techniques (*11, 12*) are not feasible in the x-ray range. However, information about the spatial structure of coronae can be obtained from observations of occultations of surface features either by the star itself (rotational modulation) or by the other component in a binary system (eclipse mapping). Clearly, these methods use less information from the incoming x-ray flux and hence provide less information on the spatial distribution of the active regions. Basically, one tries to infer a two-dimensional or even three-dimensional intensity distribution, effectively an image of a stellar corona, from the measurement of a one-dimensional light curve; the mathematics of the light curve inversion usually leads to an ill-posed problem, the solution of which requires special care.

Eclipse studies at x-ray wavelengths have been carried out for the eclipsing RS CVn systems AR Lac (*13–15*), ER Vul (*16*), and TY Pyx (*17*), for the eclipsing dMe pair YY Gem (*18*), and for the Algol system β Per (*19*). In all previously studied eclipsing systems, with the exception of β Per (where no eclipses have been found), both components are known to contribute to the total x-ray flux, which exacerbates the problem of assigning the x-ray flux to a binary component and determining coronal structure. Furthermore, RS CVn systems consist of two evolved, late-type stars with considerably larger radii and rotation rates than the sun, and YY Gem consists of a pair of very rapidly rotating M dwarfs, which are much smaller than the sun; therefore, no solarlike star has so far been studied for coronal structure.

For eclipse mapping, an ideal system consists of a smaller x-ray–bright and a larger x-ray–dark component. During eclipse ingress (egress) of the x-ray–dark component, the x-ray–bright component is gradually covered up (uncovered), giving rise to small jumps in the x-ray light curve when individual emitting regions are crossed; the whole situation resembles very much the case of a solar eclipse observed in integrated light at x-ray wavelengths (*20*). Thus, one would like to observe an eclipsing binary system consisting of a late-type dwarf star (preferably of spectral type G, like the sun) and a main-sequence A-type star or a giant M-type star. Whereas systems of the latter kind are difficult to find on evolutionary grounds, systems of the former type are not unusual.

The nearest known binary system to satisfy all those requirements is the system α CrB. A primary component of spectral type A0V and a secondary component of spectral type G5V are in an eccentric orbit (e = 0.37) of 17.36 days. The system shows photometric eclipses, with primary eclipse (G star in front of A star) being annular and secondary eclipse (A star in front of G star) being total; further, the system is a double-lined spectroscopic binary. The radii of the binary components can thus be determined to be 3.0 and 0.9 solar radii for the A and G components, respectively, and a full solution of the orbit motion (including the orbit inclination) can be obtained (*21*).

Whereas an earlier study (*22*) failed to detect x-ray emission from α CrB, with an upper luminosity limit of 4×10^{28} erg/s, the system was detected in the ROSAT all-sky survey. We therefore obtained further x-ray observations of α CrB during secondary (optical) eclipse. We used the PSPC onboard ROSAT (*23*).

The x-ray light curve (Fig. 1) shows an obvious eclipse between phases 0.945 and 0.956. An inspection of the individual photons recorded between those times in comparison with the expected background count rates shows that the eclipse is consistent with being total (that is, no source x-ray flux). Therefore, the contribution of the A-type primary star to the total x-ray flux in the α CrB system must be negligible, in accordance with expectations (*4, 24*). We derived an upper limit of 0.02 for the x-ray flux ratio of the two components.

From the out-of-eclipse count rate of α CrB, 0.17 counts per second, we estimate the total x-ray luminosity of $\sim 6 \times 10^{28}$ erg/s, more than one order of magnitude larger than the typical soft x-ray luminosity of the sun. If the total x-ray output from α CrB were attributable to solarlike active regions, most of the star's surface would have to be covered with active regions, implying a coronal filling factor near unity. With the corona modeled as a uniformly emitting disk, a light curve drawn as the solid curve in Fig. 1 would result. The observed x-ray light curve is inconsistent

Max-Planck-Institut für Extraterrestrische Physik, 85740 Garching, Federal Republic of Germany.

with such a model. If this discrepancy were attributable to an incorrect ephemeris, a timing error of ~1.3 hours would be suggested. However, even if the phase of the model light curve is optimally shifted, no satisfactory fit to the data can be obtained with a uniform disk model. We conclude that the deviations of the observed x-ray light curve from symmetry (Fig. 1) provide direct evidence for the spatial inhomogeneity of the corona of α CrB B; we wish to emphasize, however, that the detailed distribution of surface inhomogeneities does sensitively depend on the assumed ephemeris.

The most dramatic changes in count rate occur during the observation intervals 1 and 5 (Fig. 2) when a region located in the fourth quadrant of the stellar disk (the G-star region with negative x and y coordinates in Fig. 2) is covered up and uncovered, respectively. We conclude that most of the x-ray flux from the α CrB G star must come from this region; this conclusion is solely derived from the eclipse geometry and therefore does not depend on the detailed coronal modeling adopted. If the increase in count rate at the end of the fourth viewing interval is taken to be real, a relatively small emission feature may be located close to the stellar limb in the first quadrant.

Next, we constructed specific two-dimensional intensity distributions for the corona of α CrB B; because of the upper limit to the equatorial rotation velocity of $v_{eq} < 14$ km/s (21), the rotation of the G star during our eclipse measurement was insignificant, and hence, we could not obtain any stereoscopic information. We were able to model the x-ray light curve (in analogy to the modeling of optical photometric waves) quite well with two or three circular emission regions; however, the sizes of these regions were not tightly constrained, and it is not clear to what extent the derived errors reflect uncertainties resulting from the data or uncertainties from the modeling procedure (because α CrB's active regions are not likely to be circular).

To avoid such ambiguities, we adopted a nonparametric modeling procedure: We first divided the total out-of-eclipse x-ray flux from α CrB (I_{tot} = 0.17 counts per second) into N "flux quanta" of equal size: $I_i = I_{tot}/N$ for $i = 1$ to N. Next, we divided the (projected) surface into M equal (projected) pixels b_j, $j = 1$ to M. A specific corona model is then specified by a given distribution of the N flux quanta over the M spatial bins (by specifying K_j, $j = 1$ to M, where K_j is the number of flux quanta in spatial bin j); obviously, $\Sigma_{j=1}^{M} K_j = N$ must hold. Observations are available at phases ϕ_ℓ, $\ell = 1$ to S, where S is the number of observations; from the known eclipse geometry, we can calculate $v_{j,\ell}$, the fraction of the pixel j visible at phase ℓ; obviously, we must have $0 \leq v_{j,\ell} \leq 1$ for any pixel j and phase ℓ. The expected number of counts at phase ℓ is then given by

$$n_{ex,\ell} = \frac{I_{tot}}{N} \sum_{j=1}^{M} (v_{j,\ell} K_j t_\ell) + b_\ell \qquad (1)$$

where t_ℓ and b_ℓ denote the exposure time and expected background count of phase bin ℓ. The observed number of counts in phase bin ℓ, $n_{ob,\ell}$, should then be Poisson distributed with expectation value $n_{ex,\ell}$, and the best fit coronal model K_j, $j = 1$ to M, is one that makes the observed photon distribution $n_{ob,\ell}$, $\ell = 1$ to S the most likely one, given K_j, $j = 1$ to M. This best model can be found by minimizing the test statistic

$$L = -2 \log(P) = -2 \sum_{\ell=1}^{S} [-n_{ex,\ell} + n_{ob,\ell} \log(n_{ex,\ell})] \qquad (2)$$

where we have introduced the likelihood (instead of probability P) in the usual way.

Finding the coronal structure is now a problem of combinatorial optimization. Although the number of different coronal models (the set of occupation numbers K_j, $j = 1$ to M) is finite, finding the optimal solution is not trivial because of the large number of possible models ($\sim M^N$). Furthermore, the optimal solution by itself is almost meaningless because a larger number of similar and possibly even quite different models may exist that produce similarly acceptable fits to the observed x-ray light curve. The method of optimization by simulated annealing (OSA) appears to be well suited to both determine a solution close to optimum as well as characterize all solutions with a goodness of fit similar to the optimum-fit solution (25–27). We adopted an annealing schedule similar to a previously suggested one (25).

The function to be minimized is given by Eq. 2. We chose N = 121 flux quanta and M = 169 bins; with this choice, a circle can be divided into equal areas, each of which is given by an annular sector with $r_{out} - r_{in} = (2/11)\, r_{circle}$, and the central bin is a circle with radius $(1/11)\, r_{circle}$. The first 121 pixels cover the stellar disk, whereas the remaining 48 pixels define a ring

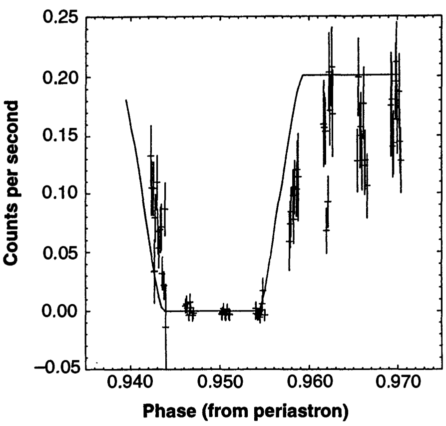

Fig. 1. The PSPC light curve of α CrB, binned into 200-s bins, versus phase with respect to stellar periastron computed from the parameters given in table 2 of Tomkin and Popper (*21*). The observations were carried out on 12 July 1992 between 4:23 and 16:15 UT. The center of secondary eclipse was predicted at 9:30 UT. The solid line represents the light curve expected from a uniformly bright corona extending over the stellar disk. Because of various operational constraints such as South Atlantic Anomaly passage and earth blocks, during which observations of celestial x-ray sources are not possible, ROSAT cannot obtain continuous x-ray light curves. The data have been corrected for all instrumental effects, including dead time, and are background subtracted.

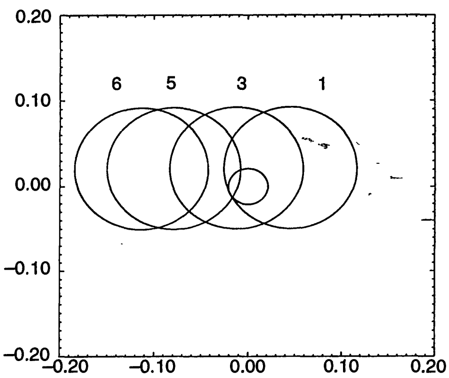

Fig. 2. Representative eclipse geometry of the light curve in Fig. 1. The G star is kept fixed (small circle in the center); the large circles represent the position of the x-ray–dark A star during ROSAT orbits 1, 3, 5, and 6 (corresponding to four of the eight clusters of data in Fig. 1). The observation started with most of the G star already eclipsed; at the end of the first viewing interval, the G star was fully occulted (circle 1). Inspection of the individual photon arrival times showed that during the last 50 s, no photons arrived; thus, the data are consistent with the G star's corona having been fully eclipsed. During orbits 2, 3, and 4, the G star was fully occulted behind the A star, and eclipse egress started a few hundred seconds before the end of the third viewing interval. There was no significant source signal above background during these times. During the fourth observation interval, eight photons were recorded with 5.5 expected from background; the last six out of the eight recorded photons did, however, arrive during the last 400 s of this interval, so it is possible (though not required) to interpret this also as the start of the x-ray eclipse egress. By the time of the fifth interval, most of the G star disk was uncovered (circle 5), and intervals 6, 7, and 8 were outside optical eclipse. Note that the scale is arbitrary.

around the star with $r_{in} = r_{star}$ and $r_{out} = (13/11)\ r_{star}$. In this fashion, we allow for the possibility of a corona extending over the stellar disk, while at the same time, we can also account for the special case of a uniform disk. We start the minimization procedure with a random distribution, that is, from a chance realization of a uniform distribution. Starting from very different randomly produced initial distributions, we convinced ourselves that the annealing procedure converges to essentially the same minimum regardless of the initial conditions; to put it differently, it appears that the combinatorial minimization problem (Eq. 1) has only one solution characterized by some L_{min} (Eq. 2). The expected light curve calculated from the best model found with our annealing scheme (Fig. 3) is an obvious improvement over the curve for a uniform disk (Fig. 1).

In Fig. 4 we show the eclipse map that results in the best fit light curve shown in Fig. 3. Clearly, this best possible solution of Eq. 2 and the derived image remain to some extent meaningless unless all other solutions that are close to the optimal solution in likelihood can be characterized. We defined other acceptable solutions as those solutions with $L - L_{min} < 1$ and, starting from the optimal solution, made random spatial redistributions of the flux bins $j = 1$ to N subject to the condition $L - L_{min} < 1$. Because our optimal solution can be reached by the annealing scheme regardless of the initial conditions, this procedure will statistically sample all valid solutions of Eq. 2. From more than 10,000 different models subject to the constraint $L - L_{min} < 1$, we proceeded to calculate the mean number of flux bins per spatial pixel and found that such a map looks very similar to the one in Fig. 4. This suggests that Fig. 4 is a good representation of all maps yielding an acceptable light curve fit.

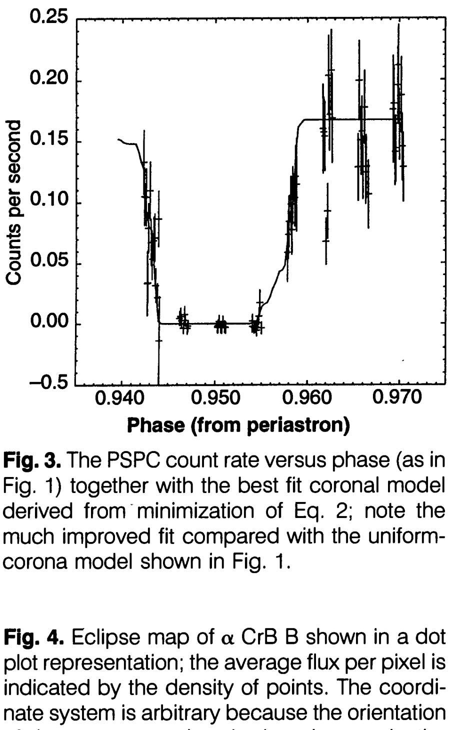

Fig. 3. The PSPC count rate versus phase (as in Fig. 1) together with the best fit coronal model derived from minimization of Eq. 2; note the much improved fit compared with the uniform-corona model shown in Fig. 1.

The eclipse map demonstrates the asymmetry of the x-ray intensity distribution, which was already apparent from Fig. 1. Very little flux (if any) comes from outside the apparent stellar disk even though our annealing scheme was able to assign flux to pixels outside the stellar disk. We conclude that less than 10% of the total flux can come from regions outside the stellar disk. The flux from beyond the stellar disk could be zero, depending on the errors in the assumed system geometry and parameters. The flux from inside the stellar disk is concentrated into a small number of pixels. For the optimum solution, only 24 out of 169 pixels had values different from zero, and for the pixels covering the stellar surface, only 10 out of 121 pixels were different from zero. Only 11 out of 169 pixels have more than one flux quantum, and 80% of the total flux appears to come from 7 pixels in total, 6% of the surface. In other words, the coronal filling factor of α CrB B is small.

No eclipse map can reproduce all of the spatial structure of the corona of α CrB B. One spatial dimension is lost by projection, and although structure in the dimension along the motion of the eclipsing A star (the x axis in Fig. 4) can be reconstructed quite well, structure perpendicular to the direction of motion can be reconstructed only with some difficulty because pixels with identical or similar eclipse geometry are located in crescentlike regions on the star. The flux (expressed in percent of the total flux) from regions A, B, C, and D (defined in Fig. 4) amounts to 45, 31, 8, and 8%, respectively, with less than 10% of the total flux coming from outside the stellar disk. The spatial morphology of the active regions is consistent with low-latitude activity belts [which are known to characterize x-ray–emitting active regions on the sun (24)] if the rotation axis of α CrB B is more or less perpendicular to the orbit plane.

Almost half of the total coronal flux comes from a rather small region, which may not even be resolved in our map (the smearing out of the flux along circular chords most likely arises from the eclipse geometry; see Fig. 2). For an upper limit of 1.1×10^{10} cm for the spatial extent of one pixel, and assuming the vertical size also to be given by this length scale, we obtain a volume $V < 1.5 \times 10^{30}$ cm^3 for region A and, from the reconstructed emission measure, a minimal density of $n > 2.2 \times 10^{10}$ cm^{-3}. Whereas (nonflaring) coronal loops on the sun have typical densities in the range between 2×10^9 and 4×10^9 cm^{-3}, the coronal density in α CrB B is higher by almost an order of magnitude. Therefore—to come back to the question posed in the beginning—the large x-ray luminosity of α CrB is solely a result of an increased coronal density. If the x-ray emission comes from magnetically confined loops, we can apply the loop scaling laws (28) to infer, with a typical temperature of $\sim 4 \times 10^6$ K as measured from the PSPC pulse height spectrum, the characteristic loop length scales as $\sim 10^9$ cm. This is consistent with our view that the high-intensity regions revealed in our eclipse map are not individual loops but rather represent active region complexes consisting of a multitude of loops.

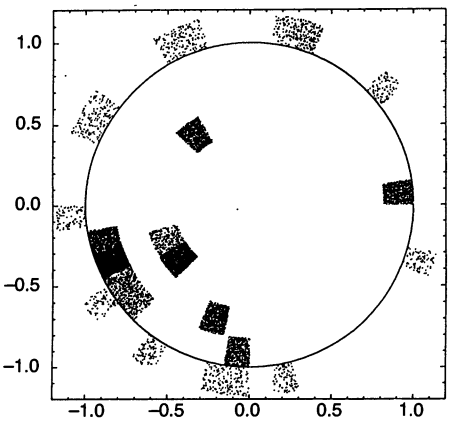

Fig. 4. Eclipse map of α CrB B shown in a dot plot representation; the average flux per pixel is indicated by the density of points. The coordinate system is arbitrary because the orientation of the system on the sky is unknown. In the chosen system, the eclipsing A star moves along the line $y = 1$ from right to left. The apparent stellar disk of the G star is plotted as a solid circle. Note the extremely spotty appearance of this stellar corona with its small filling factor. Considering the eclipse geometry of the pixels with significant flux, we conclude that the four pixels along the left rim of the star very likely constitute one active region (region A) on α CrB B; the same applies to the four pixels extending from (−0.5,−0.2) to (0.0,−1.0), which we interpret as a second active region B; the pixel located at (−0.3,0.4) probably and the pixel located at (1.0,0.0) certainly represent additional regions C and D. Note that the scale is in units of stellar radii.

REFERENCES AND NOTES

1. G. S. Vaiana *et al.*, *Astrophys. J.* **245**, 163 (1981).
2. J. H. M. M. Schmitt, in *Cool Stars, Stellar Systems, and the Sun*, M. S. Giampapa and J. A. Bookbinder, Eds. (ASP Conference Ser., Astronomical Society of the Pacific, San Francisco, CA, 1992), vol. 26, p. 83.
3. L. Golub *et al.*, *Astrophys. J.* **271**, 264 (1983).
4. J. H. M. M. Schmitt *et al.*, *ibid.* **290**, 307 (1985).
5. J. L. Linsky and B. M. Haisch, *ibid.* **229**, L27 (1979).
6. T. R. Ayres, J. L. Linsky, G. S. Vaiana, L. Golub, R. Rosner, *ibid.* **250**, 293 (1981).
7. B. M. Haisch and T. Simon, *ibid.* **263**, 253 (1982).
8. R. Rosner, L. Golub, G. S. Vaiana, *Annu. Rev. Astron. Astrophys.* **23**, 413 (1985).
9. L. Golub *et al.*, *Nature* **344**, 842 (1990).
10. L. Acton *et al.*, *Science* **258**, 618 (1992).
11. S. S. Vogt, G. D. Penrod, A. P. Hatzes, *Astrophys. J.* **321**, 496 (1987).

12. M. Kürster, *Astron. Astrophys.* **274**, 851 (1993).
13. F. M. Walter, D. M. Gibson, G. S. Basri, *Astrophys. J.* **267**, 665 (1983).
14. N. E. White, R. A. Shafer, K. Horne, A. N. Parmar, J. L. Culhane, *ibid.* **350**, 776 (1990).
15. R. Ottmann, J. H. M. M. Schmitt, M. Kürster, *ibid.* **413**, 710 (1993).
16. N. E. White, J. L. Culhane, A. N. Parmar, M. A. Sweeney, *Mon. Not. R. Astron. Soc.* **227**, 545 (1987).
17. J. L. Culhane, N. E. White, R. A. Shafer, A. N. Parmar, *ibid.* **243**, 424 (1990).
18. B. M. Haisch, J. H. M. M. Schmitt, M. Rodonó, D. M. Gibson, *Astron. Astrophys.* **230**, 419 (1990).
19. N. E. White *et al.*, *Astrophys. J.* **301**, 262 (1986).
20. P. L. Bornmann and L. D. Matheson, *Astron. Astrophys.* **231**, 525 (1990).
21. J. Tomkin and D. M. Popper, *Astron. J.* **91**, 1428 (1986).
22. J. H. M. M. Schmitt *et al.*, *Astrophys. J.* **351**, 492 (1990).
23. J. Trümper *et al.*, *Nature* **349**, 579 (1991).
24. J. H. M. M. Schmitt, in *Proceedings of the G. S. Vaiana Memorial Symposium "Advances in Stellar and Solar Coronal Physics,"* J. L. Linsky and S. Serio, Eds. (Kluwer, Dordrecht, Netherlands, in press).
25. S. Kirkpatrick, C. D. Gelatt Jr., M. P. Vecchi, *Science* **220**, 671 (1983).
26. D. G. Bounds, *Nature* **329**, 215 (1987).
27. W. Jeffrey and B. Rosner, *Astrophys. J.* **310**, 473 (1986).
28. R. Rosner, W. H. Tucker, G. S. Vaiana, *ibid.* **220**, 643 (1978).

6 May 1993; accepted 11 August 1993

Confinement of Electrons to Quantum Corrals on a Metal Surface

M. F. Crommie, C. P. Lutz, D. M. Eigler

A method for confining electrons to artificial structures at the nanometer lengthscale is presented. Surface state electrons on a copper(111) surface were confined to closed structures (corrals) defined by barriers built from iron adatoms. The barriers were assembled by individually positioning iron adatoms with the tip of a 4-kelvin scanning tunneling microscope (STM). A circular corral of radius 71.3 Å was constructed in this way out of 48 iron adatoms. Tunneling spectroscopy performed inside of the corral revealed a series of discrete resonances, providing evidence for size quantization. STM images show that the corral's interior local density of states is dominated by the eigenstate density expected for an electron trapped in a round two-dimensional box.

When electrons are confined to lengthscales approaching the de Broglie wavelength, their behavior is dominated by quantum mechanical effects. Here we report the construction and characterization of structures for confining electrons to this lengthscale. The walls of these "quantum corrals" are built from Fe adatoms which are individually positioned on the Cu(111) surface by means of a scanning tunneling microscope (STM). These adatom structures confine surface state electrons laterally because of strong scattering that occurs between surface state electrons and the Fe adatoms. The surface state electrons are confined in the direction perpendicular to the surface because of intrinsic energetic barriers that exist in that direction (*1*). Since similar surface states exist on all noble metals (*2–6*), we expect that the behavior reported here is not unique to Cu.

One quality that separates these new structures from quantum dots formed from semiconductor heterostructures is that the quantum states of the corrals may be resolved spatially as well as spectroscopically. Analysis of the spatial and spectroscopic properties of a ring of 48 Fe adatoms reveals that this corral is well described by solutions to Schrödinger's equation for a particle in a hard-wall enclosure. Despite this agreement, however, the details of the confinement mechanism are not completely understood.

The experiments were performed with an STM contained in ultrahigh vacuum and cooled to 4 K (*7, 8*). Operation at low temperature provided the stability, cleanliness, and absence of thermal diffusion of adsorbates required for this experiment. The single-crystal Cu sample was prepared by repeated cycles of Ar ion sputtering and annealing. The Auger-clean sample was then cooled to 4 K and dosed with a calibrated electron-beam Fe evaporator (0.005 monolayer coverages were typical). The convention used here is that the bias across the tunnel junction (V) is the voltage of the sample measured with respect to the tip. dI/dV spectra were measured through lock-in detection of the ac tunnel current driven by a 205-Hz, 10-mV (rms) signal added to the junction bias. All STM images were acquired in the constant current mode with a polycrystalline tungsten wire as the STM tip.

The confinement property of the Fe adatom structures derives from the scattering of surface state electrons by Fe adatoms. The results of this scattering can be seen in Fig. 1A, which shows a 130 Å × 130 Å STM image of a single Fe adatom on the Cu(111) surface (acquired with a bias of 0.02 V). The local density of states (LDOS) at E_F surrounding the adatom is marked by a circular standing wave pattern caused by the interference of incident and scattered surface state electrons (*5*). Figure 1B shows a cross sectional slice of the adatom image, more clearly displaying the 15 Å period oscillations.

If the Fe adatom is modeled as a cylindrically symmetric scattering potential, then the change in surface LDOS around the adatom is determined by the partial wave phase shifts of the scattered surface state electrons. At low energies, the change in LDOS far from the Fe adatom can be approximated as (*5*)

$$\Delta\mathrm{LDOS}(\rho) \propto \frac{1}{k\rho}\left(\cos^2\left(k\rho - \frac{\pi}{4} + \delta_0\right) - \cos^2\left(k\rho - \frac{\pi}{4}\right)\right) \quad (1)$$

where $k = (2m^*E/\hbar^2)^{1/2}$. Here δ_0 is the phase shift of the $l = 0$ scattered wave, m^* is the effective mass of a surface state electron (0.38 m_e) (*2, 5, 9*), and E is the energy measured from the surface state band-edge. By fitting Eq. 1 to our linescan data (as shown in Fig. 1B), we find that the Fe scattering strength at E_F can be characterized by an $l = 0$ phase shift of $\delta_0 = -80° \pm 5°$, which indicates strong scattering.

The strong scattering of surface state electrons by Fe adatoms suggests that they would be good building blocks for constructing microscopic electron confinement structures. In order to test this idea, we used the adatom "sliding" process (*7, 10*) to position individual Fe adatoms into orderly structures on the Cu(111) surface (bias parameters during the slide process were 0.01 volt and 5×10^{-8} amp). Figure 2A shows an STM image of 48 Fe atoms that have been positioned into a ring. This image was taken at a bias of 0.01 V. The ring has a mean radius of 71.3 Å, and the spacing between neighboring Fe atoms varies from 8.8 Å to 10.2 Å (*11*). A striking feature of Fig. 2A is the strong modulation of the LDOS inside of the Fe ring. Figure 2B shows a linescan taken through the center of the ring.

A standard method for characterizing an electronic system is to measure its density of states via tunneling spectroscopy (*12*). With an STM this is done by measuring the differential conductivity (dI/dV) of the tunnel junction (*13*). Figure 3 shows dI/dV spectra measured with the STM tip centered over different points on the surface. The top curve shows the spectrum measured with the tip held over a Cu terrace about 1000 Å away (laterally) from the Fe ring. This spectrum is relatively featureless, with the dominant characteristic being a

IBM Research Division, Almaden Research Center, 650 Harry Road, San Jose, CA 95120–6099.